1996

Hamiltonian Chaos IV

Nicolas Regez

Wolfgang Breymann

Stefan Weigert

Charles Kaufman
University of Rhode Island, ckaufman@uri.edu

Gerhard Müller
University of Rhode Island, gmuller@uri.edu

Citation/Publisher Attribution

N. Regez, W. Breymann, S. Weigert, C. Kaufman, and G. Müller. *Hamiltonian chaos IV*. Computers in Physics **10** (1996), 39-45.
Available at: http://dx.doi.org/10.1063/1.168560

Hamiltonian Chaos IV

The following article appeared in Computers in Physics and may be found at http://dx.doi.org/10.1063/1.168560.

Hamiltonian Chaos IV

Nicolas Regez[*], Wolfgang Breymann[*], Stefan Weigert[*],
Charles Kaufman[†], and Gerhard Müller[†]

[*]Institut für Physik, Universität Basel, CH-4056 Basel, Switzerland
[†]Department of Physics, University of Rhode Island, Kingston, RI 02881-0817

Configuration space, phase space, Hilbert space. Where is the real world? Where are the laws of physics at work? Is chaos a question of the space just as "high treason is a question of the date" (Talleyrand)?

Consider a double pendulum. The two-dimensional (2D) configuration space is a disk-shaped rink. The inner pendulum bob moves forward or backward on a circular path, regularly or irregularly in time, while the outer bob traces a complicated figure that may reach any point on the disk. In 4D phase space the two bobs are represented by a single phase point. This point moves forward at all times and never intersects its own path. It may trace a closed trajectory (1D object), an invariant torus (2D object), or a more complicated structure that does not fit on any 2D manifold. In Hilbert space the dimensionality is infinite, and the state of the double pendulum is represented by a unit vector performing an elaborate pirouette.

Trajectories that look messy in configuration space may or may not have that appearance in phase space. The term *chaos* is reserved for a jumble in phase space. In part I of this series[1] we employed classical Poincaré surfaces of section in order to describe chaos in phase space. In parts II and III we investigated Hamiltonian chaos from a global perspective by using classical and quantum invariants as computed from trajectories in phase space or from state vectors in Hilbert space, respectively.

In this fourth part of the series, we adopt a more local perspective by using a suitable phase space description of quantum states. We shall study *quantum Poincaré surfaces of section* for individual eigenstates of an integrable or nonintegrable system with two degrees of freedom. The eigenstates will be represented in the form of *Husimi distributions* in phase space. Husimi distributions of quantum states in turn will be constructed from *coherent states*. In the following, we introduce these concepts on an elementary level and then tackle the systems we discussed in parts I–III, namely two-spin clusters.

Consider the quantum harmonic oscillator,

$$\hat{H} = \frac{\hat{p}^2}{2m} + \frac{1}{2}m{\omega_0}^2\hat{q}^2 = \hbar\omega_0(\hat{a}^\dagger\hat{a} + \frac{1}{2})\,. \tag{1}$$

The position and momentum operators with $[\hat{q},\hat{p}] = i\hbar$ and the bosonic creation and annihilation operators with $[\hat{a},\hat{a}^\dagger] = 1$ are linearly related to each other:

$\hat{q} = \sqrt{\hbar/2m\omega_0}(\hat{a}^\dagger + \hat{a})$, $\hat{p} = i\sqrt{\hbar m\omega_0/2}(\hat{a}^\dagger - \hat{a})$. The states $|n\rangle$, $n = 0, 1, 2, \ldots$, defined by the relations $\hat{a}^\dagger|n\rangle = \sqrt{n+1}|n+1\rangle$, $\hat{a}|n\rangle = \sqrt{n}|n-1\rangle$, are the eigenstates of (1): $\hat{H}|n\rangle = \hbar\omega_0(n + \frac{1}{2})|n\rangle$.

Because the operators $\hat{p}, \hat{q}$ do not commute, their values in any given state of the system are subject to the Heisenberg uncertainty relation,

$$\langle(\Delta\hat{p})^2\rangle\langle(\Delta\hat{q})^2\rangle = (\langle\hat{p}^2\rangle - \langle\hat{p}\rangle^2)(\langle\hat{q}^2\rangle - \langle\hat{q}\rangle^2) \geq \frac{1}{4}|\langle[\hat{p}, \hat{q}]\rangle|^2 = \frac{1}{4}\hbar^2 . \tag{2}$$

Therefore, the closest thing to a phase point we can express in quantum mechanical terms is a wave function that is localized in both the position and momentum representations such that (2) is satisfied with the equality sign. Coherent states are a set of states with this minimum-uncertainty property.

The ground state $|0\rangle$ of the harmonic oscillator is a coherent state. The minimum-uncertainty property can be verified by using, for example, the familiar ground-state wave function in the q-representation,

$$\psi_0(q) = \big(\frac{m\omega_0}{\pi\hbar}\big)^{\frac{1}{4}} e^{-m\omega_0 q^2/2\hbar}, \tag{3}$$

which has the form of a Gaussian localized at $q = 0$ in configuration space. In the p-representation, it also is a Gaussian, localized at $p = 0$. The phase space coordinates of the peak position provide a natural specification of this coherent state: $|n = 0\rangle = |q = 0, p = 0\rangle$. All the other coherent states can be generated from this particular one by a translation which shifts the average position $\langle\hat{q}\rangle$ and the average momentum $\langle\hat{p}\rangle$ from $(0, 0)$ to an arbitrary point (q, p) in phase space. This transformation is implemented by an operator in the form of an exponentiated creation operator,^{2}

$$|q, p\rangle = e^{-\frac{1}{2}|z|^2} e^{\bar{z}\hat{a}^\dagger}|0, 0\rangle. \tag{4}$$

The endpoint of the shift is specified by the complex number $z = \big[q\sqrt{m\omega_0} - ip/\sqrt{m\omega_0}\big]/\sqrt{2\hbar}$ (see Problem 1). For the evaluation of expectation values we expand the exponential operator in a power series to obtain

$$|q, p\rangle = e^{-\frac{1}{2}|z|^2} \sum_{n=0}^{\infty} \frac{1}{\sqrt{n!}} \bar{z}^n |n\rangle , \tag{5}$$

where $\bar{z}$ is the complex conjugate of z.

The Husimi distribution in phase space of any (stationary or nonstationary) quantum state $|\psi\rangle$ is defined by its overlap with the two-parameter family of coherent states:

$$W_\psi(q, p) = |\langle q, p|\psi\rangle|^2 . \tag{6}$$

For the eigenstates $|n\rangle$ of the harmonic oscillator, we obtain

$$W_n(q, p) = \frac{1}{n!}|z|^{2n} e^{-|z|^2} . \tag{7}$$

We have plotted W_n in Fig. 1a for the ground state and two excited states of the harmonic oscillator. Since the eigenstates are stationary, their Husimi distributions are time-independent.

Recall that the classical phase portrait of the harmonic oscillator is a dense set of ellipses with the fixed point at the center representing the classical ground state. The Husimi distribution of the quantum ground state is a 2D Gaussian centered at the same point. The nonzero width of the distribution reflects the quantum uncertainty requirement (2). The Husimi distributions of the excited states are rim-like objects with their ridges along the classical trajectories. These phase space structures may be called quantized invariant tori as discussed in part III.

Unlike the eigenstates $|n\rangle$, the coherent states $|q,p\rangle$ are generally nonstationary. The time-dependent Husimi distribution of the nonstationary coherent state

$$|q_0,p_0,t\rangle = e^{-\frac{1}{2}|z_0|^2}\sum_{n=0}^{\infty}\frac{1}{\sqrt{n!}}\bar{z}_0^n e^{-i(n+\frac{1}{2})\omega_0 t}|n\rangle \tag{8}$$

reads

$$W_{q_0,p_0}(q,p,t) = |\langle q,p|q_0,p_0,t\rangle|^2 = e^{-|z-z_0e^{i\omega_0 t}|^2}\ . \tag{9}$$

The peak of this localized distribution travels on a closed elliptic path with period $2\pi/\omega_0$, much like the corresponding classical phase point. Note that the distribution (9) does not diffuse (see Problem 2). Figure 1b depicts three snapshots of one coherent state taken at successive times (see Problem 3).

When this analysis is carried out for an *anharmonic oscillator*, the calculational demands increase substantially. Equation (5) for the coherent state $|q,p\rangle$ remains unchanged, but the harmonic oscillator states $|n\rangle$ are no longer eigenstates. We express the new eigenstates in the form $|\psi_l\rangle = \sum_{n=0}^{\infty} c_{ln}|n\rangle$, $l = 0,1,2,\ldots$ The resulting (time-independent) Husimi distributions can be written in the form

$$W_l(q,p) = \left|\sum_{n=0}^{\infty}\frac{c_{ln}}{\sqrt{n!}}z^n\right|^2 e^{-|z|^2}\ . \tag{10}$$

Under anharmonic time evolution, coherent initial states lose the minimum-uncertainty property. If our goal is to determine the (time-dependent) Husimi distribution for a state $|q_0,p_0,t\rangle$ which is coherent at $t=0$, we need to express the (nonstationary) harmonic oscillator states $|n,t\rangle$ in terms of the eigenstates $|\psi_l(t)\rangle = e^{-iE_lt/\hbar}|\psi_l\rangle$ (see Problem 4).

In preparation of our main theme, the investigation of the eigenstates of two-spin clusters by means of quantum Poincaré maps of their Husimi distributions, we present here a brief introduction to coherent spin states. Consider a spin $\hat{\vec{\sigma}} = (\hat{\sigma}_x,\hat{\sigma}_y,\hat{\sigma}_z)$ with quantum number $\sigma = \frac{1}{2},1,\frac{3}{2},\ldots$ in a constant magnetic field in the z-direction,

$$\hat{H} = -\hbar\omega_0\hat{\sigma}_z, \quad \omega_0 = \frac{ge}{2mc}B\ . \tag{11}$$

The spin components satisfy $[\hat{\sigma}_\alpha,\hat{\sigma}_\beta] = i\hat{\sigma}_\gamma$ for $(\alpha\beta\gamma) = \mathrm{cycl}(xyz)$. The eigenstates $|m\rangle$, $m = -\sigma,-\sigma+1,\ldots,\sigma$ of (11) are defined by the relations $\hat{\sigma}_z|m\rangle =$

$m|m\rangle$, $\hat{\sigma}_\pm|m\rangle = \sqrt{(\sigma \mp m)(\sigma \pm m+1)}|m\pm 1\rangle$, where $\hat{\sigma}_\pm = \hat{\sigma}_x \pm i\hat{\sigma}_y$. The quantum spin length $\hbar\sqrt{\sigma(\sigma+1)}$ is determined by the relation $\hat{\vec{\sigma}}^2|m\rangle = \sigma(\sigma+1)|m\rangle$.

A natural parametrization of spin coherent states is provided by the angular coordinates (ϑ, φ) of the mean spin direction as inferred from the relation $(\langle\hat{\sigma}_x\rangle, \langle\hat{\sigma}_y\rangle, \langle\hat{\sigma}_z\rangle) = \sigma(\sin\vartheta\cos\varphi, \sin\vartheta\sin\varphi, \cos\vartheta)$. The lowest and highest spin eigenstates $|\pm\sigma\rangle$ happen to be stationary coherent spin states, and for the ground state of (11) we write[3] $|m = +\sigma\rangle = |\vartheta = 0,\ \varphi = 0\rangle$. All other coherent spin states can be generated from this state by a rotation of the (mean) spin direction away from the north pole to an arbitrary direction specified by the polar angle ϑ and the azimuthal angle φ. This rotation is implemented by a unitary operator of the form[4]

$$|\vartheta, \varphi\rangle = e^{-i\vartheta(\hat{\sigma}_x \sin\varphi - \hat{\sigma}_y \cos\varphi)}|0, 0\rangle. \qquad (12)$$

In analogy to (5), it is useful to express the rotated coherent state as a linear combination of the spin eigenstates:

$$\begin{aligned} |\vartheta, \varphi\rangle &= \sum_{m=-\sigma}^{+\sigma} d_m(\vartheta, \varphi)|m\rangle, \\ d_m(\vartheta, \varphi) &= \sqrt{\frac{(2\sigma)!}{(\sigma+m)!(\sigma-m)!}}\, e^{-i\varphi(\sigma-m)}[\sin\frac{\vartheta}{2}]^{\sigma-m}[\cos\frac{\vartheta}{2}]^{\sigma+m}. \end{aligned} \qquad (13)$$

Husimi distributions for arbitrary spin states $|\psi\rangle$ are calculated as in (6) for the oscillator case: $W_\psi(\vartheta, \varphi) = |\langle\vartheta, \varphi|\psi\rangle|^2$. For the eigenstates $|m\rangle$ of (11), we obtain stationary Husimi distributions of the form $W_m(\vartheta, \varphi) = |d_m(\vartheta, \varphi)|^2$, which are independent of the azimuthal angle φ. These distributions are best visualized as the height above sea level on a globe (see Problem 5).

The nonstationary coherent spin states $|\vartheta_0, \varphi_0, t\rangle$ for the simple model (11) can be determined analogously to (8). Their time-dependent Husimi distributions all have exactly the same shape, namely that of the state $|0, 0\rangle$, but are rotated to the initial angular position (ϑ_0, φ_0). They all move rigidly and synchronously at constant latitude around the globe. The minimum-uncertainty property is again preserved in time.

In a generic one-spin Hamiltonian, the spin states $|m\rangle$ are not stationary. With the eigenvectors $|\psi_l\rangle = \sum_{m=-\sigma}^{+\sigma} c_{lm}|m\rangle$, $l = 0, \ldots, 2\sigma$, and their energy eigenvalues E_l obtained from a numerical diagonalization, we can express the Husimi distributions $W_l(\vartheta, \varphi)$ analogously to (10) in terms of the expansion coefficients c_{lm}. If we use the matrix $\{\gamma_{lm}\}$, the inverse of the matrix $\{c_{lm}\}$, to express the time evolution of the basis vectors $|m, t\rangle = \sum_{l=0}^{2\sigma} \gamma_{ml}\, e^{-iE_l t/\hbar}|\psi_l\rangle$, and use (13), we can write the time evolution of the state $|\vartheta_0, \varphi_0, t\rangle$ as

$$|\vartheta_0, \varphi_0, t\rangle = \sum_{ml} d_m(\vartheta_0, \varphi_0)\gamma_{ml} e^{-iE_l t/\hbar}|\psi_l\rangle. \qquad (14)$$

Note that $|\vartheta_0, \varphi_0, t\rangle$ starts out at $t = 0$ as a coherent state centered at (ϑ_0, φ_0). We can then determine the time-dependent Husimi distribution $W_{\vartheta_0,\varphi_0}(\vartheta, \varphi, t) = |\langle\vartheta, \varphi|\vartheta_0, \varphi_0, t\rangle|^2$.

As an illustration, we consider the one-spin Hamiltonian

$$\hat{H} = \hbar\omega_0(\hat{\sigma}_y - \hat{\sigma}_z) - \hbar^2 D \hat{\sigma}_x^2 \,. \tag{15}$$

Its classical counterpart, $H = \omega_0(S_y - S_z) - DS_x^2$, generates an anharmonic time evolution of the spin components $(S_x, S_y, S_z) = s(\sin\vartheta\cos\varphi, \sin\vartheta\sin\varphi, \cos\vartheta)$, which is specified (for $\omega_0 = 1, D = 1$) by the equations of motion

$$\frac{dS_x}{dt} = S_z + S_y, \quad \frac{dS_y}{dt} = -S_x + 2S_xS_z, \quad \frac{dS_z}{dt} = -S_x - 2S_xS_y. \tag{16}$$

In Fig. 2a we show several trajectories generated by (16). The phase points move in the direction of the arrows. The four fixed points (where $dS_x/dt = dS_y/dt = dS_z/dt = 0$) are readily identified in this phase portrait: two elliptic points at $(60°, -35.3°)$ and $(60°, -144.7°)$ with clockwise flows around them; one hyperbolic point between the two at $(45°, -90°)$; and a third elliptic point at $(135°, 90°)$ with anticlockwise flow around it. Classical trajectories are lines of constant energy. When interpreted as a contour plot of the classical energy, Fig. 2a depicts a landscape with a mountain peak of height $E = \sqrt{2}$ on the lower right and two ocean troughs of depth $E = -3/2$ on the upper left, separated by a saddle point at $E = -\sqrt{2}$.

We can construct the corresponding quantum phase portrait by mapping out the (ϑ, φ)-strip according to the average energy,

$$\langle\vartheta, \varphi|\hat{H}|\vartheta, \varphi\rangle = \sum_l E_l |\sum_m d_m(\vartheta, \varphi)\gamma_{ml}|^2 \tag{17}$$

of the coherent state peaked at (ϑ, φ). Figure 2b shows contours of this function for four values of σ. The four panels reproduce the classical energy topography of Fig. 2a with different degrees of resolution. The double well, for example, does not exist on the quantum energy topographic map for very small spin quantum numbers. The limited resolution is attributable to quantum uncertainty.

To complete the quantum phase diagram, we need to attribute a sense of direction to any line segment of constant average energy. We choose a coherent state centered at some point on a given line of constant average energy and determine the direction in which the peak of its Husimi distribution moves in time. This determination cannot be done without ambiguity, again due to quantum uncertainty. Figure 3 depicts snapshots at successive times of Husimi distributions corresponding to three initial coherent states.

Consider the state initially centered at $(40°, 120°)$. Its Husimi distribution, shown in the form of a color-coded density plot, remains localized during the time interval shown. The peak position follows the line of constant average energy very closely. It undergoes a periodic motion very much like the corresponding classical phase point and with almost the same period. Very similar observations are made if we pick the initial coherent state at $(126°, 74°)$. The Husimi distributions of this state at four successive instants are shown by the contour plots on the lower right of Fig. 3. A different scenario arises if we pick the initial coherent state at $(46°, -86°)$ near the classical separatrix. This

Husimi distribution does not stay localized as time evolves. Different parts of it move along lines of constant average energy on opposite sides of the hyperbolic point as shown by the contour plots on the upper left of Fig. 3.

The flow of the Husimi distribution is akin to that of a classical phase space density with a comparable degree of localization. The quantum flow pattern for initial coherent states suggests a sense of direction along the lines of constant average energy in Fig. 2b which is consistent with the classical flow pattern in Fig. 2a, but the quantum uncertainty imposes an intrinsic limit to the degree of localization.

These results demonstrate that the universal integrability of autonomous (classical) systems with one degree of freedom is reflected with remarkable clarity in individual stationary and nonstationary states of the corresponding quantum systems. The Husimi distributions of energy eigenstates tend to be concentrated in the immediate vicinity of the classical torus for that energy, and the Husimi distributions of (initially) coherent states tend to stay localized and move with a velocity similar to that of a classical phase point on the torus of the same energy. However, the quantum uncertainty requirements render this correspondence fuzzy in those regions of phase space where the classical time evolution is most sensitive to small changes in initial conditions.

Now we turn to systems with two degrees of freedom, which may or may not be integrable. Integrability guarantees a fully intact 2D torus structure in the 4D phase space. Nonintegrability implies that a fraction of the tori is destroyed and replaced by chaotic trajectories. By what characteristic patterns does the classical integrability or nonintegrability manifest itself in the Husimi distributions of eigenstates of the corresponding quantum system? By what kind of graphical representation can these patterns be displayed for direct comparison with classical Poincaré maps, where the effects of integrability and nonintegrability are clear cut and readily verified?

To answer the second question, we use a *quantum Poincaré map*, which in essence is a classical Poincaré map applied to the (smooth) Husimi distribution $W_l(q_1, p_1, q_2, p_2)$ of a quantum eigenstate in contrast to the (highly singular) phase space density $P(q_1, p_1, q_2, p_2)$ of a single classical trajectory. The classical Poincaré map chosen here for comparative purposes is implemented as follows: Any given initial phase point (q_1, p_1, q_2, p_2) traces a trajectory on the 3D energy hypersurface $H(q_1, p_1, q_2, p_2) = E_{\rm cl} = \text{const}$. This invariant reduces the number of independent coordinates in the phase space density $P(q_1, p_1, q_2, p_2)$ from four to three. A further reduction from three to two is imposed by considering only those points where a trajectory intersects the 3D hyperplane $p_2 = 0$ with $\dot{p}_2 < 0$. These points are plotted in a diagram of the two remaining independent coordinates (q_1, p_1). Each dot in such a diagram can be interpreted as a δ-function contribution to the Poincaré map of the phase space density of a single trajectory. For regular trajectories the dots tend to accumulate along piecewise smooth lines, whereas for chaotic trajectories they tend to spread in a 2D region of the (q_1, p_1) diagram (see parts I and II).

For direct comparison with these classical structures, individual eigenstates $|\psi_l\rangle$ of the corresponding quantum Hamiltonian are graphically represented by applying the same reduction of variables to their Husimi distributions $W_l(q_1, p_1, q_2, p_2)$. As in the one-spin problem, we use angular coordinates ϑ, φ in place of the canonical variables q, p. Hence, we express the quantum Poincaré map as $\overline{W}_l(\vartheta_1, \varphi_1) = W_l(\vartheta_1, \varphi_1, \vartheta_2 = \pi/2, \varphi_2 = \bar{\varphi}_2)$, where $\bar{\varphi}_2$ is determined by the (classical) requirements $E_{\rm cl} = {\rm const}$ and $\dot{\vartheta}_2 > 0$. The function $W_l(\vartheta_1, \varphi_1, \vartheta_2, \varphi_2)$ can be determined from the spin coherent states $|\vartheta_1, \varphi_1, \vartheta_2, \varphi_2\rangle$ and the spin eigenstate $|\psi_l\rangle$ by a straightforward generalization of the procedure outlined in the context of the one-spin model.

Panels (a)–(c) of Fig. 4 show density plots of the quantum Poincaré map $\overline{W}_l(\vartheta_1, \varphi_1)$ for three eigenstates $|\psi_l\rangle$ of the *integrable* two-spin Hamiltonian

$$\hat{H}_\gamma = \hbar^2 \big[(1+\gamma)\hat{\sigma}_{1x}\hat{\sigma}_{2x} + (1-\gamma)\hat{\sigma}_{1y}\hat{\sigma}_{2y}\big] \tag{18}$$

with $\gamma = 0.5$ and for spin quantum number $\sigma = 151/2$. Panel (d) depicts the classical Poincaré map of several trajectories at energy $E_{\rm cl} = -0.1$ for the same model. The three quantum eigenstates have energies very close to $E_{\rm cl}$. Note the similarity in shape of the corresponding classical and quantum stationary objects in this common representation. The eigenstates accurately outline the shapes of the invariant tori.[5] In panel (a) we have chosen the eigenstate with the largest (squared) projection $|\langle\psi_l|\vartheta_1, \varphi_1, \pi/2, \bar{\varphi}_2\rangle|^2$ onto the spin coherent state centered at the location of the four elliptic fixed points on the line $\vartheta_1 = \pi/2$ belonging to one (stable) periodic trajectory. The eigenstate selected for panel (b) is the one with the largest value $\overline{W}_l(\vartheta_1, \varphi_1)$ at the two hyperbolic fixed points located on the same line ($\vartheta_1 = \pi/2$) and belonging to a single (unstable) periodic trajectory. The eigenstate depicted in panel (c) traces an invariant torus far from any fixed point.

The Husimi distributions of the eigenstates of $\hat{H}_\gamma$ tend to remain localized near the corresponding classical invariant tori. In part II we pointed out that each classical torus in a fully intact foliation is specified by two global action coordinates. In part III we used quantum invariants to show that eigenstates of an integrable two-spin model are naturally labeled by two quantum numbers representing quantized actions. The results of Fig. 4 now demonstrate the close relationship between quantum eigenstates and classical invariant tori on an individual basis.

Different structures in quantum Poincaré maps are expected for the *nonintegrable* two-spin Hamiltonian

$$\hat{H}_\alpha = \hbar^2 \big[\hat{\sigma}_{1x}\hat{\sigma}_{2x} + \hat{\sigma}_{1y}\hat{\sigma}_{2y} + \frac{1}{2}\alpha\{(\hat{\sigma}_{1x})^2 - (\hat{\sigma}_{1y})^2 + (\hat{\sigma}_{2x})^2 - (\hat{\sigma}_{2y})^2\}\big]. \tag{19}$$

Our results for $\alpha = 0.5$ and $\alpha = 0.7$ are displayed in Figs. 5 and 6, respectively. We have used the same combination of plots as in Fig. 4. The classical Poincaré map of Fig. 5d shows that chaos is conspicuous but considerably constrained by intact tori. There exists a broad band of chaos around the regular island centered at the primary elliptic fixed points and connecting the primary hyperbolic fixed points on the line $\vartheta_1 = \pi/2$. Within that chaotic region, we can detect four regular islands of intact tori winding around secondary elliptic fixed points.

How clearly are these prominent classical structures reflected in the quantum Poincaré maps of individual eigenstates at nearby energies? The states shown in Figs. 5a and 5b are the ones with maximum projection onto the coherent states centered at the above mentioned primary and secondary elliptic fixed points, respectively. Their distributions $\overline{W}_l(\vartheta_1, \varphi_1)$ stay localized around these (stable) fixed points. The eigenstate shown in Fig. 5c, by contrast, which has the strongest overlap with the coherent state centered at the primary hyperbolic fixed point of Fig. 5d, has a much less localized distribution $\overline{W}_l(\vartheta_1, \varphi_1)$. It spreads into a region on the quantum Poincaré map which outlines the range of the chaotic region on the classical Poincaré map in remarkable detail.

At $\alpha = 0.7$ the classical phase flow of $\hat{H}_\alpha$ is considerably more widespread than at $\alpha = 0.5$, as can be seen on the classical Poincaré map depicted in Fig. 6d. Most of the invariant tori which were still present at $\alpha = 0.5$ have now melted into a wide sea of chaos interspersed with small islands of tori around certain elliptic fixed points. Even under these very chaotic circumstances there are quantum eigenstates that are localized tightly near these islands of stability. Figs. 6a and 6b show the quantum Poincaré maps of two such states. But then there are other eigenstates at almost the same energy which spread to nearly all regions on the quantum Poincaré map. The distribution $\overline{W}_l(\vartheta_1, \varphi_1)$ of the state depicted in Fig. 6c has its largest value at the (unstable) hyperbolic fixed point.

The coexistence of two kinds of eigenstates in nonintegrable quantum systems, namely those which are akin to quantized tori and those which resemble chaotic trajectories on the Poincaré map, have also been identified in parts II and III. There the torus structure was represented quantum mechanically by an invariant-web. In the integrable model $\hat{H}_\gamma$, all states were found to be part of the fully intact fabric, whereas in the nonintegrable model $\hat{H}_\alpha$, the fabric was shown to be partially torn. By means of the Poincaré maps of Figs. 5 and 6, we now have a close-up view of these two kinds of eigenstates and their properties in a phase space representation. Chaos is not a question of how the state of the system is represented, but the analytical and graphical instruments required to recognize and explore chaos vary widely in different representations.

Suggested Problems for Further Study

1. The definition of the operator for a general translation in the (q, p)-plane is $\hat{T} = e^{i(p\hat{q} - q\hat{p})/\hbar}$. Show that the application of this operator on the ground state of the harmonic oscillator yields Eq. (4) after normalization of the resulting state.

2. Determine the expectation values $\langle \hat{q} \rangle$, $\langle \hat{p} \rangle$, and the uncertainty product $\langle (\Delta\hat{p})^2 \rangle \langle (\Delta\hat{q})^2 \rangle$ for the coherent state (8) of the harmonic oscillator from the Husimi distribution (9). Compare the result for $\langle (\Delta\hat{p})^2 \rangle \langle (\Delta\hat{q})^2 \rangle$ with the right-hand side of (2). Also determine the uncertainty product for the coherent state $|\vartheta_0, \varphi_0\rangle$ of the one-spin Hamiltonian (11) by the same method. In this case the integral is over a sphere and the integration variables are $p = s\cos\vartheta, q = \varphi$.

3. On the phase plane with rescaled axes $\tilde{q} = q\sqrt{m\omega_0/2\hbar}$, $\tilde{p} = p/\sqrt{2\hbar m\omega_0}$, the peak of the Husimi distribution (9) traces a circle. Relate the radius for the classical oscillator to the average energy of the coherent state. Establish the corresponding relation between the energy and the radius of the classical oscillator. Compare the two relations.

4. Consider the anharmonic oscillator $\hat{H} = \hat{p}^2/2m + (m\omega_0^2/2)\hat{q}^2[\alpha + \beta m\omega_0\hat{q}^2/\hbar]$. Use the harmonic-oscillator states $|n\rangle$ as a basis for the matrix representation of this Hamiltonian. Find the eigenvectors and eigenvalues for the matrix truncated at $n_T = 10, 20, \ldots$ With increasing n_T there will be a growing number of eigenvalues, $E_l, l = 1, \ldots, l_T$, which are very little affected by the truncation of $\hat{H}$. Pick a coherent state $|q_0, p_0\rangle$ whose average energy is well within the range of energy eigenvalues for which truncation is not a problem. Use the procedure described in the text to calculate the time-dependent Husimi distribution in a suitable representation. Interpret the time evolution of the coherent state in light of the classical phase portrait. Carry out the calculation and analysis for several different initial coherent states and for parameter values of $\hat{H}$ which include single-well and double-well potentials.

5. Plot the Husimi distribution $W_m(\vartheta, \varphi)$ for various eigenstates $|m\rangle$ of the one-spin model (11) in a spherical representation. The state $|\sigma\rangle$ will be represented by a localized peak at the north pole and states with $-\sigma < m < \sigma$ by ring-shaped bulges at constant latitude. Demonstrate that the angular width of these structures decreases with increasing spin quantum number and goes to zero in the classical limit, $\hbar \to 0, \sigma \to \infty, \hbar\sqrt{\sigma(\sigma+1)} = s$.

Acknowledgments. The research in Basel was supported by Schweizerischer Nationalfonds and the research at URI by the U. S. National Science Foundation, Grant DMR-93-12252. Access to computing facilities at the NCSA at Urbana-Champaign and at the CSCS in Manno, Switzerland is gratefully acknowledged. We thank Harvey Gould and Jan Tobochnik for helpful suggestions. N. R. would like to thank H. Thomas and especially W. Breymann for instructive discussions.

References

1. N. Srivastava, C. Kaufman, and G. Müller, *Comput. Phys.* **4**, 549 (1990), *ibid.* **5**, 239 (1991); *ibid.* **6**, 84 (1992). These columns are referred to as I, II, and III, respectively.

2. P. Leboeuf and M. Saraceno, *J. Phys.* **23**, 1745 (1990) and references therein.

3. The uncertainty in spin direction is a direct consequence of the non-commutativity of the spin components $\hat{\sigma}_x$, $\hat{\sigma}_y$, $\hat{\sigma}_z$, which implies the inequalities $\langle(\Delta\hat{\sigma}_\alpha)^2\rangle\langle(\Delta\hat{\sigma}_\beta)^2\rangle \geq \frac{1}{4}\langle\hat{\sigma}_\gamma\rangle^2$, $(\alpha,\beta,\gamma) = \mathrm{cycl}(xyz)$.

4. R. J. Glauber and F. Haake, *Phys. Rev.* **13**, 357 (1976) and references therein.

5. The quantum and classical structures in Figs. 4–6 can be compared in more detail if the reader makes transparent photocopies for easy superposition of any two panels.

6. N. Srivastava, C. Kaufman, G. Müller, R. Weber, and H. Thomas, *Z. Phys.* B**70**, 251 (1988).

7. N. Regez, Diplomarbeit, Universität Basel, 1993 (unpublished).

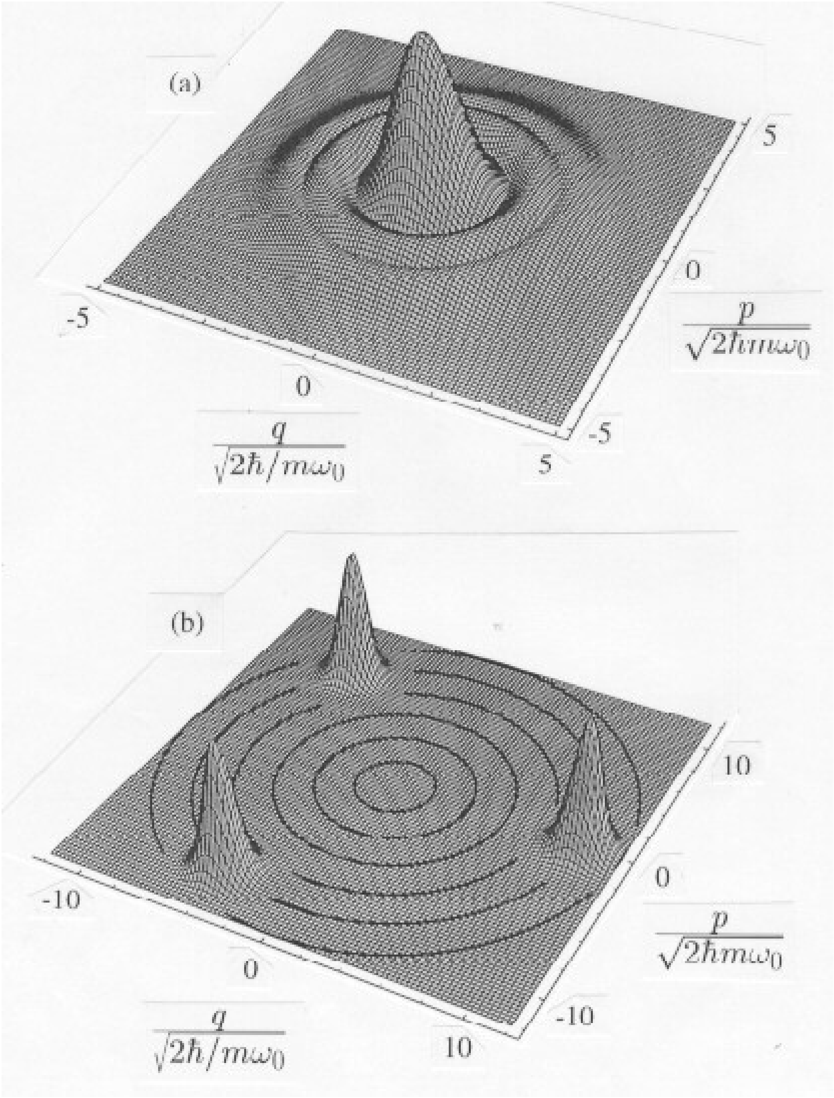

Figure 1: (a) 3D plot of the Husimi distributions (7), expressed as functions of rescaled coordinates for the ground state ($n = 0$) and two excited states ($n = 5, 9$) of the quantum harmonic oscillator. (b) 3D plot of the Husimi distributions (9) for the coherent state with initial condition $q\sqrt{m\omega_0/2\hbar} = 10$, $p/\sqrt{2\hbar m\omega_0} = 0$ at three successive times $\omega_0 t = 0, 2, 4$ of the same model.

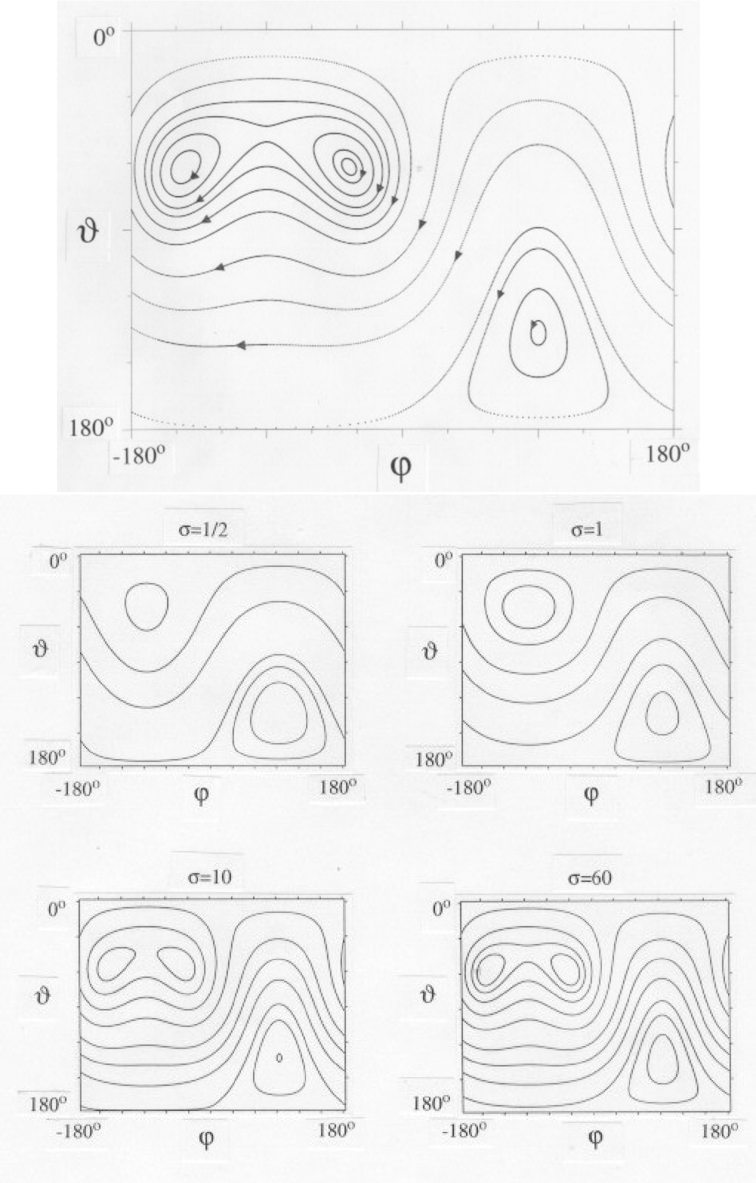

Figure 2: (a) Classical phase portrait of the one-spin model $H = S_y - S_z - S_x^2$ with $s = 1$. Each trajectory on the (ϑ, φ)-strip has been obtained by numerical integration of Eq. (16) for some initial point. (b) Contours of constant average energy of the coherent states $|\vartheta, \varphi\rangle$ for the quantum one-spin model (15) with $\omega_0 = 1, D = 1$, $\hbar = 1/\sqrt{\sigma(\sigma+1)}$, and the spin quantum numbers, $\sigma = 1/2, 1, 10, 60$.

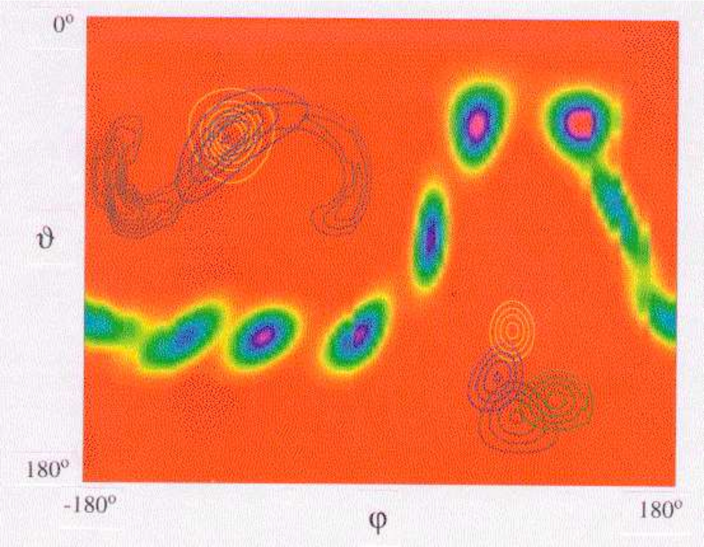

Figure 3: Husimi distributions for three nonstationary states at several successive times of the quantum one-spin model (15) with $\sigma = 60$ and $\hbar = 1/\sqrt{\sigma(\sigma+1)}$. The initial states are coherent and centered at $(46°, -86°)$, $(126°, 74°)$ (contour plots), and $(40°, 120°)$ (color-coded density plot).

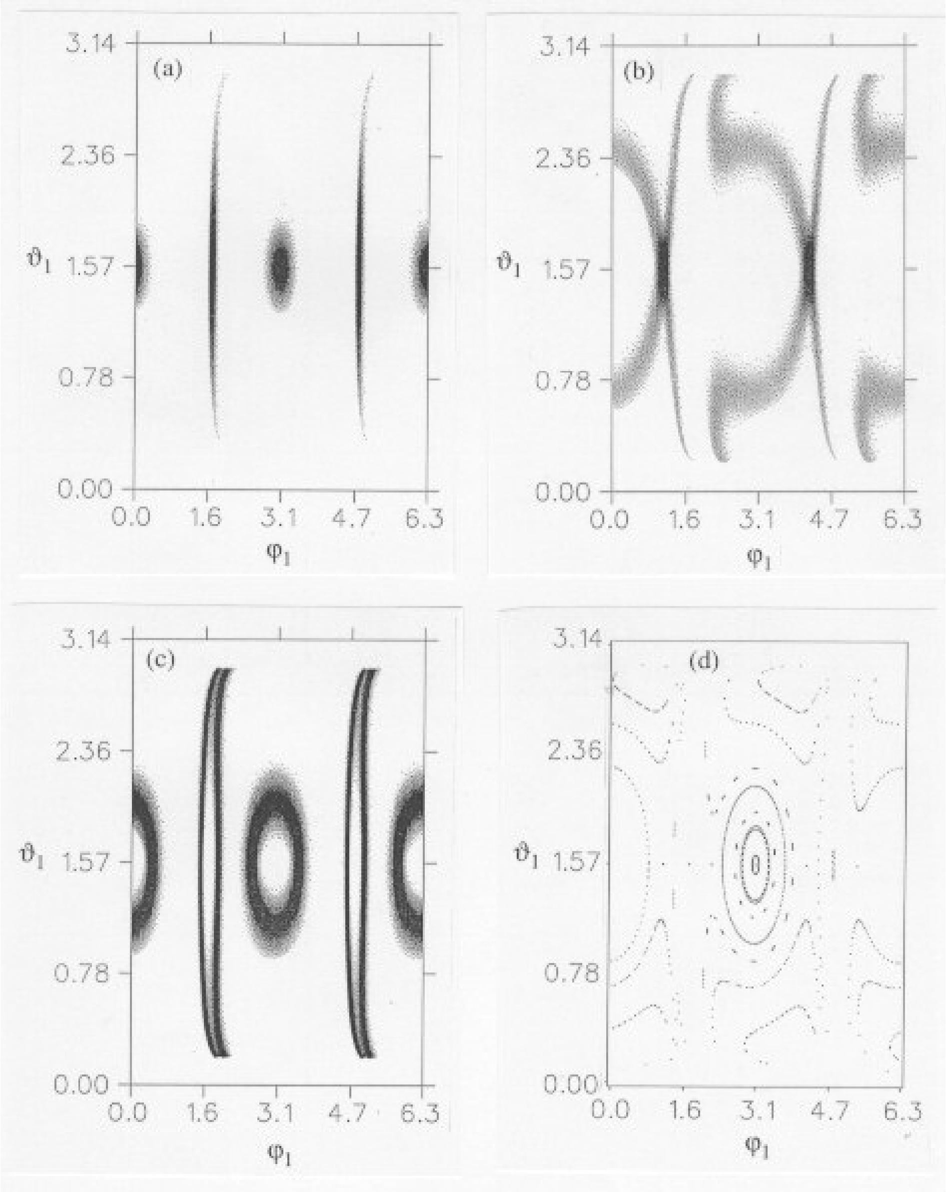

Figure 4: Quantum and classical Poincaré maps at $\vartheta_2 = \pi/2$, $\dot{\vartheta}_2 > 0$ for the integrable two-spin model (18) with $\gamma = 0.5$. Panel (d) [from Ref. 6] represents several classical trajectories at $E_{\rm cl} = -0.1$. Panels (a)–(c) [from Ref. 7] represent Husimi distributions for $\sigma = 151/2$ of three eigenstates with energies E_n very close to $E_{\rm cl}$.

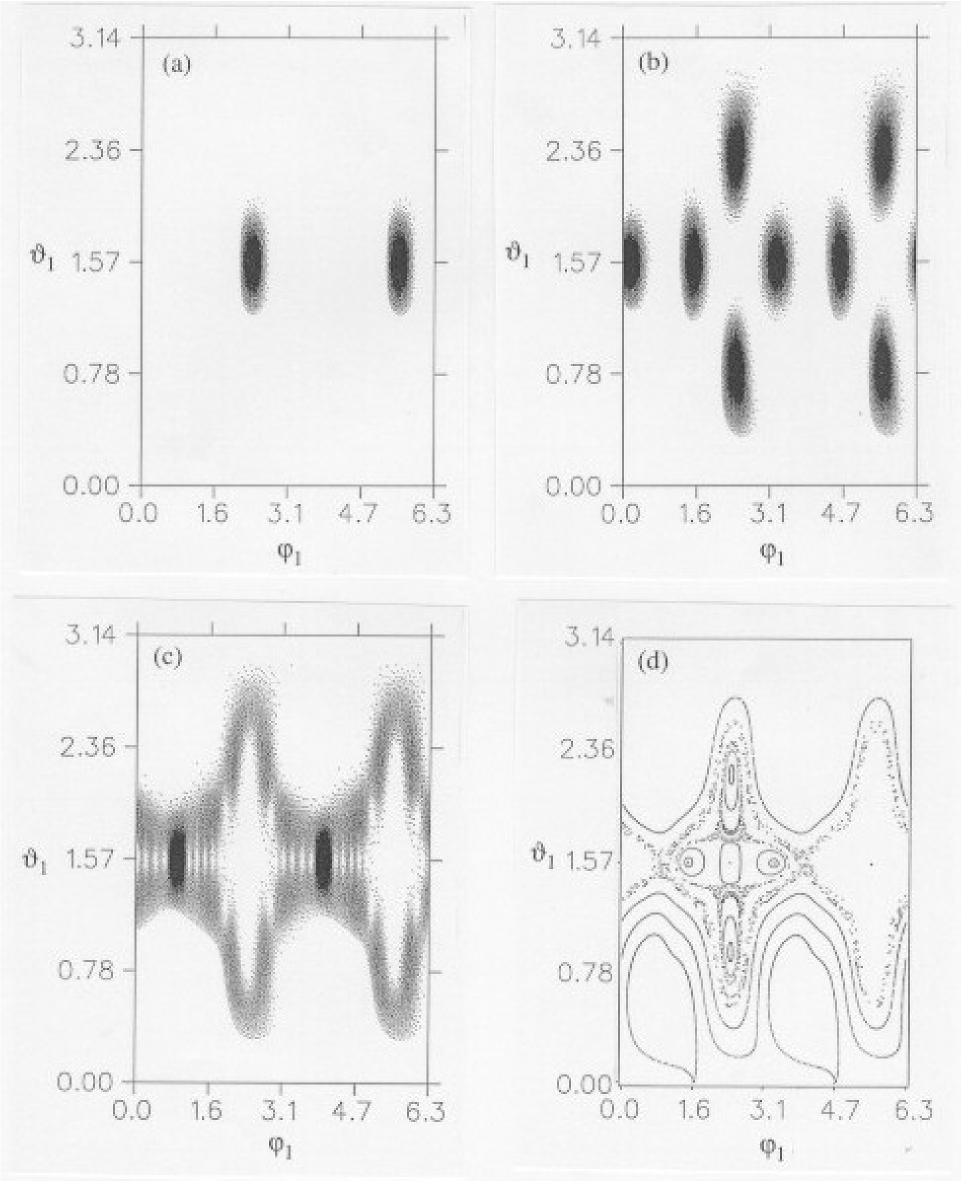

Figure 5: Quantum and classical Poincaré maps at $\vartheta_2 = \pi/2$, $\dot{\vartheta}_2 > 0$ for the nonintegrable two-spin model (19) with $\alpha = 0.5$. Panel (d) [from Ref. 6] represents several classical trajectories at $E_{\text{cl}} = -0.1$. Panels (a)–(c) [from Ref. 7] represent Husimi distributions for $\sigma = 151/2$ of three eigenstates with energies E_n very close to E_{cl}.

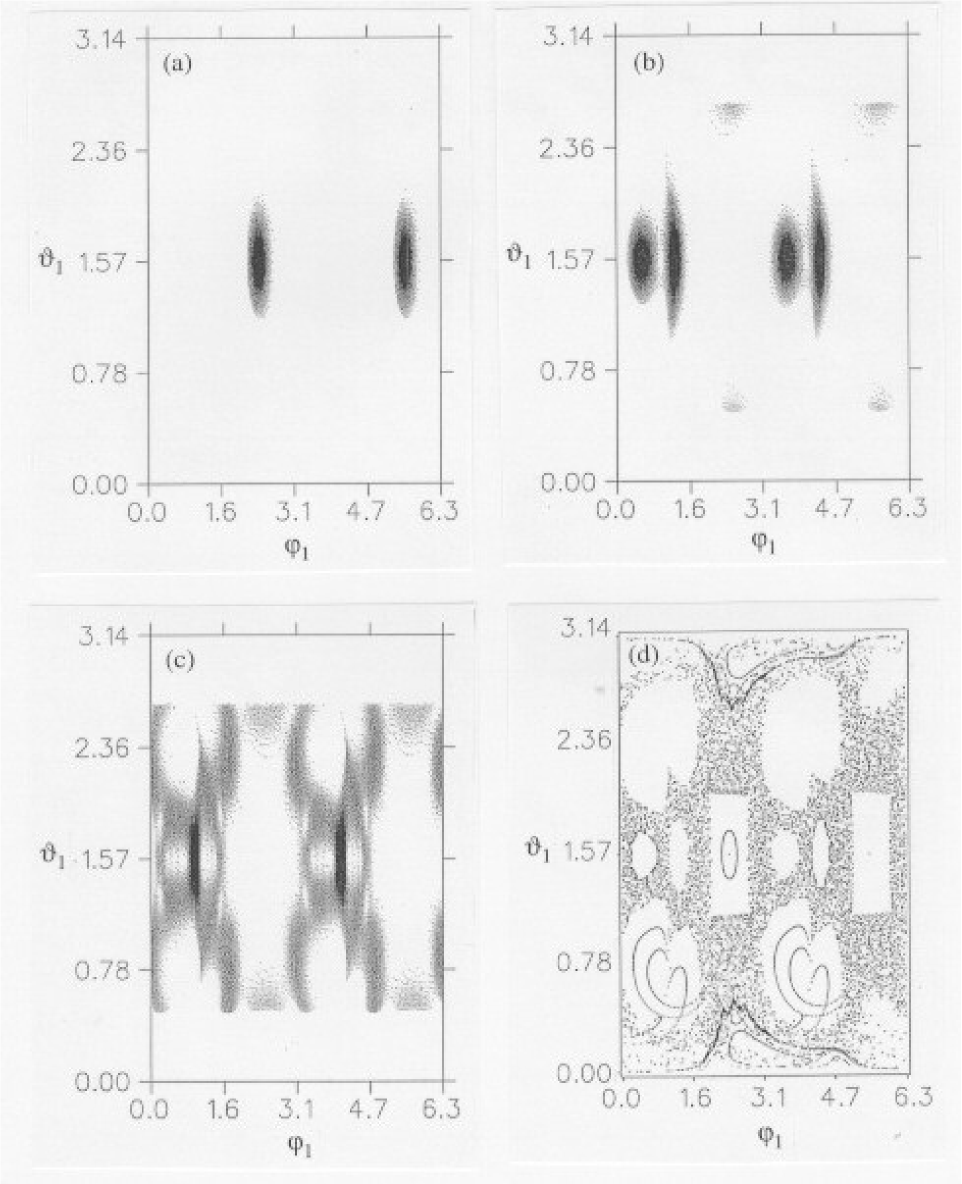

Figure 6: Quantum and classical Poincaré maps at $\vartheta_2 = \pi/2$, $\dot{\vartheta}_2 > 0$ for the nonintegrable two-spin model (19) with $\alpha = 0.7$. Panel (d) [from Ref. 6] represents several classical trajectories at energy $E_{\rm cl} = -0.1$. Panels (a)–(c) [from Ref. 7] represent Husimi distributions for $\sigma = 151/2$ of three eigenstates with energies E_n very close to $E_{\rm cl}$.